Effective Synergistic Effect of Dipeptide-Polyoxometalate-Graphene Oxide Ternary Hybrid Materials on Peroxidase-like Mimics with Enhanced Performance

Zhuo Ma,[§] Yunfeng Qiu,[*,†,‡] Huihui Yang,[‡] Yanmin Huang,[‡] Jingjing Liu,[‡] Yue Lu,[‡] Chen Zhang,[*,∥] and PingAn Hu[*,‡]

[†]State Key Laboratory of Urban Water Resource and Environment, Harbin Institute of Technology, Harbin, Heilongjiang 150090, China

[‡]Key Lab of Microsystem and Microstructure, Ministry of Education, Harbin Institute of Technology, No. 2 YiKuang Street, Harbin, Heilongjiang 150080, PR China

[§]School of Life Science and Technology, Harbin Institute of Technology, 92 West Dazhi Street, Harbin, Heilongjiang 150001, P.R. China

[∥]Department of Materials Science and Engineering, University of California, Berkeley, California 94720-1760, United States

S *Supporting Information*

ABSTRACT: Dipeptide-polyoxometalates (POMs)-graphene oxide (GO) ternary hybrid is an excellent peroxidase-like mimic, exhibiting enhanced peroxidase-like activity compared to POMs alone. The hybrid was readily prepared through a reprecipitation method involving electrostatic encapsulation of $H_3PW_{12}O_{40}$ (PW_{12}) by cationic diphenylalanine (FF) peptide and coassembly of $FF@PW_{12}$ spheres with graphene oxide (GO). Using 3,3′,5,5′-tetramethylbenzidine (TMB) as the chromogenic substrate, the peroxidase-like activity of $FF@PW_{12}$ was evaluated in the heterogeneous phase, and it is 13 times higher than that of pristine PW_{12} in the homogeneous phase. Furthermore, ternary hybrids of $FF@PW_{12}@GO$ containing 5 wt % GO could enhance the activity 1.7 times higher than that of $FF@PW_{12}$. The noncovalent interactions of hydrogen bonding and ionic interaction between GO and POMs are speculated to result in the synergistic effect for the enhancement of peroxidase-like performance. The strong interactions between rGO and PW_{12} are evaluated by a four-probe Hall measurement via the van der Pauw method, and rGO is significantly p-doped by the doping effect of PW_{12} with lower LUMO energy than that of the energy level of rGO and also due to the electron reservoir feature of PW_{12}. Cyclic voltammogram measurements also suggest that GO causes significant influence on the electronic structure of the reduced forms of the redox couples of PW_{12}. The nature of the TMB catalytic reaction may originate from the generation of the hydroxyl radical ($^•OH$) from the decomposition of H_2O_2 by ternary hybrids and the formation of peroxo species of POM. Taking advantage of the UV−vis signals of TMB being correlated to the concentration of H_2O_2, $FF@PW_{12}@GO$ can be used to detect H_2O_2 within the limit of detection of 0.11 μM, and the detection range is 1−75 μM. The present method indeed opens up a promising route in constructing heterogeneous peroxidase-like mimics through the use of POMs via the introduction of GO for building H_2O_2 sensors.

KEYWORDS: *polyoxometalates, graphene, diphenylalanine, peroxidase-like, synergistic effect*
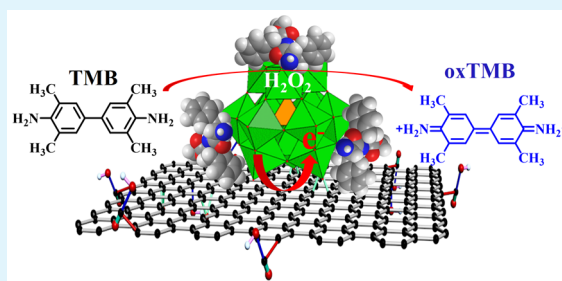
INTRODUCTION

Self-assembly is a ubiquitous phenomenon in nature at molecular and supramolecular levels, and it has been proven to be a promising and useful bottom-up approach to prepare functional materials.[1,2] To achieve desirable structures and functions, rational design of the building blocks is of great importance.[3] As an example, diphenylalanine peptide (L-Phe-L-Phe) (FF) extracted from β-amyloid polypeptide responsible for Alzheimer's disease is one of the core recognition motifs for molecular self-assembly.[4] Although facile synthesis and post-modifications have made FF readily available for constructing well-defined supramolecular structures, applications in bio-

technology and nanotechnology have been limited due to the nature of FF and very little development in FF based hybrid systems.[5−8] On the other side, a recent study showed that inorganic−organic hybrid supramolecular assemblies played a vital role in fabricating novel multifunctional materials.[9,10] Besides the intrinsic properties, supramolecular assemblies are highly desirable as they typically demonstrate cooperative functionality of the individual building blocks. As expected, the

combination of inorganic components and organic compounds may combine advantages from both elements and improve the overall performance of the resultant hybrid complexes.[11,12]

Polyoxometalates (POMs), as one of the most important inorganic building blocks, not only possess rich structural versatility such as Keggin, Wells−Dawson, Linqvist types, etc. but also demonstrate superior redox activity.[13] In particular, the ionic self-assembly (ISA) strategy, based on electrostatic interactions between two oppositely charged units, has been developed to effectively construct supramolecular structures based on negatively charged POMs.[14] Thus, novel functional materials consisting of cationic FF and anionic POMs may be constructed by applying ISA strategy.[4] In general, the enhancement of the catalytic performance of nanomaterial is directly related to the high surface area, which is easily deteriorated by coagulation of small-sized nanoaggregates during the catalysis reaction.[15] To solve the coagulation problem, dispersing these small aggregates on nanosized inorganic or polymeric supports has proven to be an effective way.[16,17]

Recently, H_2O_2 detection has attracted much attention as its production may affect many biochemistry reactions in the body that are critical for human health.[18−20] This gives us the motivation to develop efficient methods for detecting and quantifying the amount of H_2O_2 molecules in the specific system. The commonly used optical H_2O_2 detection strategy involves the use of horseradish peroxidase (HRP) catalyzing a chromogenic substrate, such as 3,3′,5,5′-tetramethylbenzidine (TMB), and a colored product will be formed.[21] Although this assay is effective, inherent drawbacks of this natural enzyme, including the sensitivity of catalytic activity to environmental changes and low operational stability, as well as time-consuming and expensive preparation and purification processes, restrict its application in various disciplines.[22,23] As a result, considerable efforts have been dedicated to design and construct novel enzyme mimics with similar functions.[24] In recent years, Fe_3O_4 magnetic nanoparticles are found to exhibit intrinsic peroxidase mimetic activity.[19,20] Many other nanomaterials such as noble metal materials,[25] metal oxides,[26] hybrid materials,[27] carbon-materials,[28,29] polymers,[30] and nanocomposites[31] have been developed, demonstrating peroxidase-like mimetic activities.

Very recently, Qu's group found that carboxylic acid (−COOH) groups modifying graphene oxide (GO) could catalyze TMB to produce a blue-colored product in the presence of H_2O_2.[28] Besides the study of intrinsic peroxidase-like activity of GO-COOH, a series of artificial enzymes use GO as supports due to facile synthesis for large-scale application, superior mechanical properties for robustness, high surface area and abundant oxygen-containing functional groups for anchoring a variety of different materials including noble metals, metal oxides, semiconductors, etc.[32−34] For example, a monolayer superlattice containing POMs on GO showed enhanced photoelectrochemical properties ascribable to the synergistic effects between the superlattice and GO.[35] Qu's group reported that both GO and AuNCs showed almost no peroxidase-like activity; however, GO/AuNCs showed superior activity, indicating the synergistic effect between AuNCs and GO.[36]

Among all the reported artificial enzymes, only a few POMs-based nanoenzymes, such as $PW_{12}O_{40}$,[37] $SiW_{12}O_{40}$,[38] and tetranuclear zirconium-substituted polyoxometalates,[39] have demonstrated enzyme mimetic activity for the detection of H_2O_2. Most of the reported POMs based peroxidase-like studies are homogeneous, suffering from recovery issue and environmental contamination. Wang et al. found that the coassembly of Fe_2SiW_{10}[40] or $PV_2Mo_{10}O_{40}$[41] with folate showed peroxidase-like activity and targeting ability toward folate acceptor overexpressed cells. However, the unsatisfied solubility of folate molecules severely hinders its coassembly with POMs. Thus, the development of biocompatible molecules encapsulated POMs complexes is highly appealing to expand the field of peroxidase mimics based on POMs. Taken together, by integrating FF, POMs, and GO into one hybrid composite, the synergistic effect among all components can potentially be realized and maximized, leading to superior performance in catalysis, energy conversion, and biotechnology. We decide to synthesize hybrids containing FF, peroxidase-active POMs, and GO because of the following reasons: 1) the introduction of FF is speculated to enhance the biocompatibility of the hybrid and the affinity toward TMB due to nonconvalent interactions; 2) strong electrostatic interactions between FF and POMs may enhance the stability in the heterogeneous phase; 3) the introduction of GO as supports may maximize the dispersion of FF/POMs hybrids and surface area of the whole composites and to enhance the affinity of TMB or H_2O_2 due to concentrating ability by aromatic regions and/or abundant oxygen-containing groups of GO on basal planes; 4) strong electron transfer between GO and POM will alter the redox property of POM.

Herein, we report the assembly behavior and characterization of FF and PW_{12} nanospheres. The nanospheres are successfully dispersed on the surface of GO. The peroxidase-like activity of FF@PW_{12} or FF@PW_{12}@GO is systematically investigated. The detection of H_2O_2 in the range from 1 μM to 75 μM is evaluated based on FF@PW_{12}@GO in detail.

■ EXPERIMENTAL SECTION

Materials and Methods. PW_{12} was purchased from Sigma-Aldrich Chemical Reagent Co., Ltd. Dipeptide NH_2-Phe-Phe-$COOCH_3$·HCl (FF·HCl) was a gift from Prof. Wujiong Xia, at Harbin Institute of Technology. ^{1}H and ^{13}C NMR spectra of FF·HCl are included in the Supporting Information, Figures S15 and S16. GO was synthesized using Hummer's method and characterized by Raman spectroscopy and AFM analysis (Figure S1, SI). GO film was prepared by a casting method on SiO_2(300 nm)/Si and then reduced by 47 wt % HI solution at 85 °C for 4 h. Three dimensional graphene (3DG) foam was synthesized according to our previous work.[42] Fourier transform infrared (FTIR) spectra of the prepared catalysts were collected on a PerkinElmer 1710 spectrometer using KBr pellet at room temperature. Contact angles were measured using the Dataphysics OCA20 CA system at ambient temperature. TGA were performed using SDT 2960, TA Instruments, with a heating rate of 10 °C·min^{-1} under N_2 atmosphere. The hydrodynamic diameters and surface potential of the hybrids were determined by dynamic light scattering (DLS) using Malvern Zetasizer Nano ZS. XRD was performed with monochromated Cu Kα radiation at a scanning rate of 2° min^{-1} in the range of 3−30° on a Rigaku D/max-γB apparatus. Scanning electron microscopy (SEM) was performed using a FEI Quanta 200 scanning electron microscope with 10 kV acceleration voltage. The sample was stuck on the observation platform and sprayed with platinum vapor under high vacuum for about 90 s. Characterization of the assemblies was performed using field emission Transmission Electron Microscopy (TEM) (Tecnai G2F30). A 0.1 mg sample was sonicated in 1 mL of H_2O for 10 min, and the solution mixture was then dropped onto a Cu grid with carbon film. An electron paramagnetic resonance (EPR, EMX-8/2.7 ESR spectrometer with ER4102ST cavity, Bruker, Germany) experiment was conducted to determine the •OH generated in the system of H_2O_2-FF@PW_{12}@GO-DMPO. A Nitron spin-

trapping reagent of 5,5-dimethyl-1-pyrolin-N-oxide (DMPO) purchased from Aladdin was used to capture •OH. All the reactions were monitored using UV−vis spectroscopy (Hitachi UV2010 spectrophotometer) in situ at 652 nm. The apparent kinetic parameters were calculated based on the equation $v = V_{max} \times [S]/(K_m + [S])$, where ν is the initial velocity, V_{max} is the maximal reaction velocity, $[S]$ is the concentration of substrate, and K_m is the Michaelis constant.[43] Hall measurements were performed at room temperature using copper pressure clips using the van der Pauw method. The clips were used as probe contacts over areas of 0.5×0.5 mm^2, and the thickness of the membrane was about 2 μm. The currents used for the measurements were 1 mA, while the magnetic induction intensity was 0.550 T. Cyclic voltammetry measurements were carried out on a CHI660D electrochemical analyzer supplied by Shanghai Chenhua Instrument Co., Ltd. (Shanghai, China). The working electrode was a glassy carbon (GC) disc and a GC disc modified by 3DG (Radius: 1.5 mm). The reference electrode was Ag/AgCl (KCl: 3 M). The auxiliary electrode was a platinum electrode. Measurements were performed in 1 M H$_2$SO$_4$ at room temperature, from approximately −0.7 V to +0.25 V at 100 mV s^{-1} for two circles.

General Procedure for the Synthesis of PW$_{12}$@FF and PW$_{12}$@FF@GO. FF·HCl powder (30 mg, 0.083 mmol) was first dissolved in 5 mL of distilled water, followed by slow addition of PW$_{12}$ aqueous solution (80 mg, 0.027 mmol in 1 mL of distilled water). The solution mixture showed a light yellow turbid suspension that was aged for 1 h. The PW$_{12}$@FF submicrospheres were assembled and filtered from the aqueous suspension and thoroughly washed three times with distilled water (50 mL × 3). The reaction yield for PW$_{12}$@FF is 65%. PW$_{12}$@FF@GO was synthesized similarly. The only modification is that the PW$_{12}$ aqueous solution contains a different weight fraction of GO. All separation processes were performed based on the above-described process, and the reaction yield for PW$_{12}$@FF@GO is 72%.

Peroxidase-like Activity of the Composites. To investigate the peroxidase-like activity of the composite, catalytic oxidation of substrate TMB in the presence of H$_2$O$_2$ was measured. In a typical colorimetric experiment, unless otherwise stated, a certain volume of catalyst aqueous dispersion (1 mg/mL) was added to 2.75 mL of an aqueous solution consisting of 50 μM TMB dispersed in 0.1 M, pH 3 buffer solution and 100 μM H$_2$O$_2$ at 60 °C. Afterward the sample in the hcuvette was positioned immediately in the cell holder of the UV−vis spectrophotometer for steady-state kinetic measurements which were implemented in time course mode by monitoring the absorbance changes at 652 nm.

■ RESULTS AND DISCUSSION

1. Morphology and Compositions. Supramolecular assemblies of FF and POMs were obtained via a reprecipitation strategy. As shown in Scheme 1, addition of the ethanol solution of PW$_{12}$ and FF in a 1:3 molar ratio into water at room temperature immediately created light suspension displaying a

Scheme 1. Schematic Illustration of the Assembly Process of the FF@PW$_{12}$@GO Complex
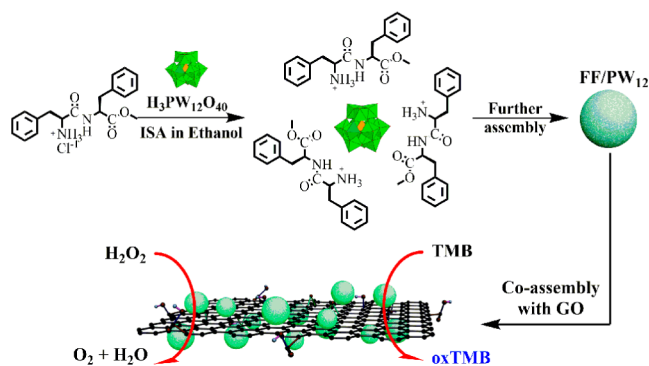
typical Tyndall effect, indicating the formation of colloidal aggregates in solution mixture. Ethanol is a good solvent for PW$_{12}$ and FF hybrids, but water is not. Thus, the introduction of water to the ethanol solution containing hybrids will likely induce the precipitation of the compounds. The suspended aggregates were characterized using SEM, and Figure 1a shows
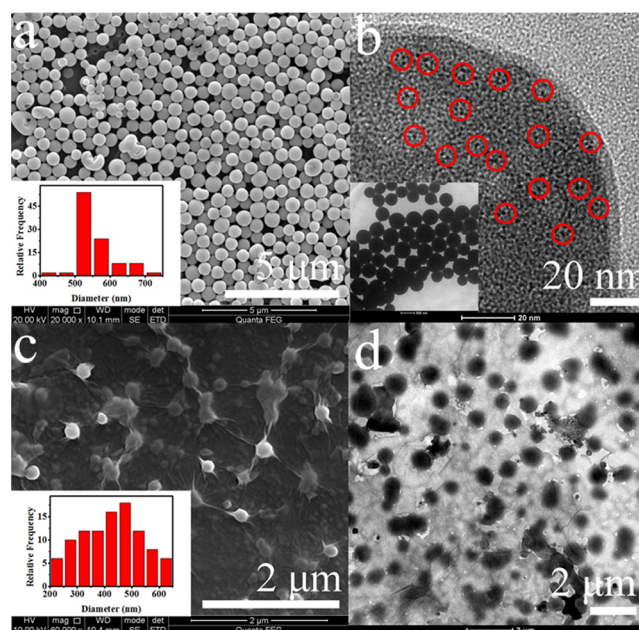

Figure 1. Characterization of hybrid hollow spheres consisting of coassembled FF and PW$_{12}$ by a) SEM (inset: statistical analysis of the size of the spheres). b) High resolution TEM image of one sphere in the inset, in which the dark spots marked by red circles with a size of ca. 1 nm are PW$_{12}$. c) SEM image of FF@PW$_{12}$@GO (5 wt %) (inset: statistical analysis of the size of the spheres). d) TEM image of FF@PW$_{12}$@GO (5 wt %).

that the aggregates are submicrospheres with an average diameter of 520 nm (inset of Figure 1a). Energy dispersive X-ray (EDS) spectroscopy (Figure S2, SI) indicates that the major elements of the submicrospheres are tungsten and carbon, indicating the successful assembly of PW$_{12}$ and FF. TEM images in the inset of Figure 1b also confirm the formation of spherical aggregates with a similar average size of ∼520 nm, both close to the hydrodynamic diameter ∼549 nm measured by DLS (Figure S3, SI).

The incorporation of PW$_{12}$ in FF forming a hybrid was confirmed using several spectroscopy techniques. Figure 2a shows the UV−vis spectra of FF, PW$_{12}$, and FF@PW$_{12}$ hybrid, respectively. The peak at 266 nm (black trace) is ascribed to the oxygen-to-metal charge transfer in PW$_{12}$, which is also observed in the FF@PW$_{12}$ hybrid. FTIR spectra of FF, PW$_{12}$, and FF@PW$_{12}$ hybrids were collected and presented in Figure 2b. As summarized in Table S1, the absorption bands of PW$_{12}$ at 1080, 984, 889, and 808 cm^{-1} are attributed to ν(P−O), ν(W═O$_t$), ν(W−O$_b$−W), and ν(W−O$_c$−W) stretching vibrations. In comparison, the same absorption bands from ν(P−O), ν(W═O$_t$), ν(W−O$_b$−W), and ν(W−O$_c$−W) stretching vibrations in FF@PW$_{12}$ hybrids changed considerably, indicating slight variations in electron distribution and structural distortion of PW$_{12}$ due to strong electrostatic interaction between PW$_{12}$ and FF. The successful introduction of FF was confirmed by the appearance of the characteristic peaks of FF at the same
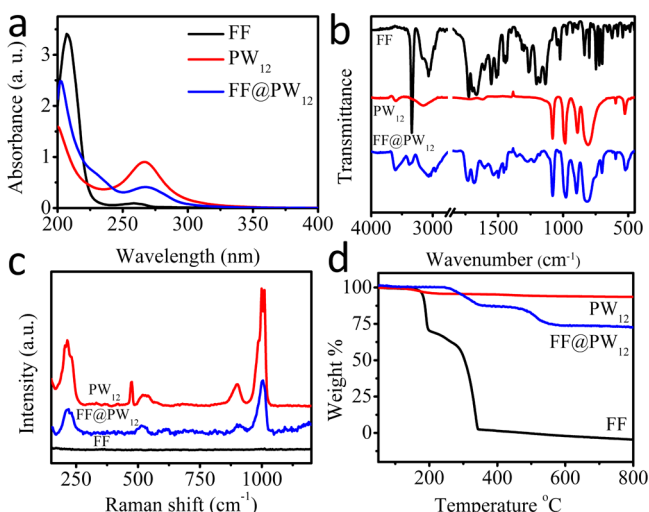
Figure 2. Characterization of FF, PW$_{12}$, and FF/PW$_{12}$ by a) UV−vis, b) FTIR, c) Raman spectroscopy, and d) TGA, respectively, confirming successful incorporation of PW$_{12}$.

positions in hybrids. Raman spectroscopy was also carried out to confirm the introduction of PW$_{12}$. As shown in Figure 3d,
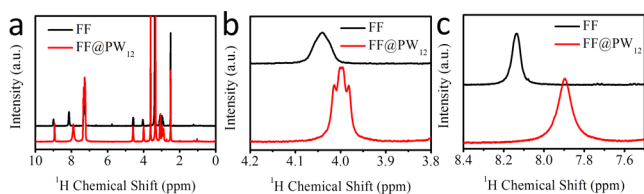

Figure 3. ^{1}H NMR spectra of (a) FF and FF@PW$_{12}$ and (b) N-methylene (N$^+$-CH$_2$) in the range from 3.8 to 4.8 ppm. (c) Protonated NH$_3^+$ in the range from 7.6 to 8.6 ppm. The interactions are confirmed to be noncovalent.

four Raman scattering peaks were found in the range of 1007−886 cm^{-1} for PW$_{12}$, corresponding to stretching vibrations of P−O bonds of the PO$_4$ sites at 1007 cm^{-1}, the W=O bond at 990 cm^{-1}, and W−O$_{b/c}$−W bonds at 920 and 886 cm^{-1} of PW$_{12}$ unit, respectively.[44] After the formation of FF@PW$_{12}$, the four Raman scattering peaks are shifted to 1004, 991, 916, 880 cm^{-1}, respectively. The FTIR and Raman spectra indicate that the primary Keggin structure of PW$_{12}$ remains intact in the hybrid, and there is electrostatic interaction between PW$_{12}$ and FF. We propose that the chemical structure for the hybrid is (NH$_3$-Phe-Phe-COOCH$_3$)$_3$PW$_{12}$O$_{40}$ with the PW$_{12}$:FF ratio being 1:3 based on charge equilibrium. TGA measurements were therefore performed to verify the proposed structure. As shown in Figure 2d, FF started to decompose above ~173 °C. TGA profile of PW$_{12}$ illustrated that the weight loss below 200 °C was attributed to the removal of physisorbed water molecules. In the case of FF@PW$_{12}$, the measured weight loss due to thermal decomposition between 240 and 800 °C is determined to be 25.42%, very close to the calculated fraction of 26.22% in the hybrid assuming the inorganic residues are WO$_3$ and P$_2$O$_5$. The starting decomposition temperature increased from 173 °C for pure FF to 240 °C for FF@PW$_{12}$, indicative of the enhanced thermal stability due to the formation of the electrostatic complex. These results reflect that the chemical structure of the hybrid is indeed as we proposed, viz, one PW$_{12}$ polyoxoanion bearing three negative

charges electrostatically combined with three FF cations as shown in Scheme 1.

From our observations so far, the synergistic effect between inorganic and organic components is highly dependent on the strong interactions between the two components. Thus, the catalytic performance of hybrids would be enhanced only when the synergistic effect is maximized. To further confirm the interaction between PW$_{12}$ and FF in solution, ^{1}H NMR was performed. As shown in Figure 3a and b, the proton chemical shifts of FF and FF@PW$_{12}$ demonstrate the following characteristics: (1) the proton signal of N-methylene (N$^+$-CH$_2$) between 3.8 and 4.8 ppm, which is a singlet in pure FF, becomes an obvious triplet and shifted toward high field by 0.05 ppm in FF@PW$_{12}$; (2) the proton peak of protonated NH$_3^+$ is significantly broadened and shifted to high field by 0.25 ppm between 7.6 to 8.6 ppm; (3) the other signals remain unchanged. The broadened peaks are speculated to be due to strong electron static interactions between FF and PW$_{12}$, which might restrict the mobility of the protonated NH$_3^+$ since the chemical shift and peak width of the proton peaks are highly dependent on the local physical and chemical environment as reported in previous work.[45] Based on the NMR analysis and the previous characterization results, we tentatively conclude that PW$_{12}$ and FF coassemble into spherical aggregates in water mainly due to the electrostatic interaction between negative PW$_{12}$ and positive FF.

Furthermore, XRD characterization for PW$_{12}$, FF, FF@PW$_{12}$, and FF@PW$_{12}$@GO are performed in Figure S4. A series of characteristic peaks are observed in the XRD pattern of PW$_{12}$ (black trace), corresponding to Keggin-type POMs. XRD pattern at wide angles from 4 to 30° indicates that FF powder possesses strong and obvious diffraction peaks, confirming ordered molecular assembly of FF molecules. However, it showed different patterns comparing with the XRD pattern of the hexagonal structure of FF single crystals.[46] FF@PW$_{12}$ and FF@PW$_{12}$@GO showed similar XRD patterns with only one sharp peak at 2θ = 6.8 and 6.7°, respectively. All of the characteristic Bragg reflections of the PW$_{12}$ and FF have disappeared. d spacing of 1.3 nm for both cases can be ascribable to the size of the one unit of (NH$_3$-Phe-Phe-COOCH$_3$)$_3$PW$_{12}$O$_{40}$ (FF$_3$PW$_{12}$) in the hybrid spheres. As roughly measured in the TEM image in Figure 1b, d spacing is consistent with the size of a basic structural unit of ~1 nm.

In addition, as shown in Figure S5, FF self-assembled into tubular structures at a concentration of 2 × 10^{-4} mol L^{-1} in ethanol at room temperature. This tubular structure is consistent with previous results.[47] It has been proposed that the well-ordered assembly of the tubular structure is possibly governed by a nucleation−growth process in the vapor−liquid−solid system during the rapid evaporation of solvent. As confirmed in XRD measurements, the ordered stacking of aromatic moieties of FF plays a key role for unidirectional growth of the tubular structure. The introduction of POM will greatly change the assembly behavior of FF. There are strong electrostatic interactions between negative PW$_{12}$ and positive FF, which are confirmed by NMR and FTIR. It is reasonable that such an electrostatic interaction might compete with an aromatic interaction responsible for the one-dimensional (1D) structure of FF and becomes prominent during the assembly of spheres.

Taken together, the loss of unidirectional growth of 1D structure is the main reason for the energetically favorable growth of spheres. (FF)$_3$PW$_{12}$ serves as a building block to

further assemble into supramolecular networks via hydrophobic interaction, van der Waals forces, and $\pi-\pi$ stacking. The assembly behavior undergoes a similar manner analogous to cationic surfactants encapsulated POMs systems.[48] Briefly, two steps are involved in the assembly of spheres. First, the building block of $(FF)_3PW_{12}$ was formed due to electrostatic interactions. Then, the supramolecular assembly of $(FF)_3PW_{12}$ occurred via noncovalent interactions.

2. Peroxidase-like Activity Evaluation. Inspired from previous work, POMs have been shown to demonstrate enzyme mimetic activity. In Wang's work, they found that PW_{12} exhibited the highest peroxidase-like activity at a concentration of 10 mM (~30 mg/mL), pH 3.0 at 55 °C. However, pristine Keggin POMs catalyze the reaction in a homogeneous way, causing recovery and contamination issues. Moreover, developments in biodetection demand very stringent requirements for the design of detecting systems. Besides sensitivity and detectivity, facile preparation process, heterogeneous nature, and biocompatibility are some characteristic features for biodetection. To evaluate whether or not our FF/PW_{12} system fulfills these requirements, the peroxidase-like activities are investigated thoroughly. The catalysis of peroxidase substrate TMB was examined in the presence of H_2O_2 with $FF@PW_{12}$ hybrid and other controls for comparison. Inset in Figure 4a
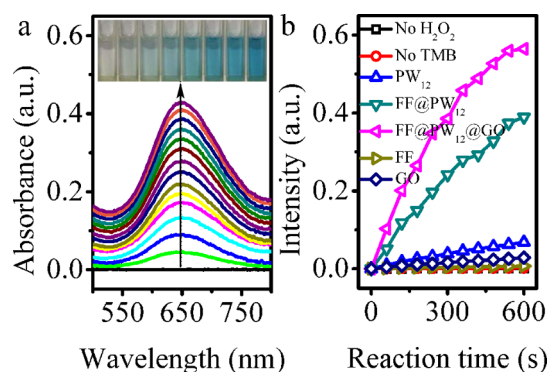

Figure 4. (a) Time dependence UV−vis spectral showing changes of the TMB-H_2O_2 system catalyzed by $FF@PW_{12}$. Inset shows the color change of the solution mixture over time in 10 min. (b) UV−vis absorption-time course curve of TMB using $FF@PW_{12}$ and other control groups.

shows the photographs of aqueous solutions of TMB with increasing reaction time in the presence of $FF@PW_{12}$. As the reaction proceeds, the color of the solution gradually changes from clear to blue in 10 min, indicating the oxidization of TMB. It is worthwhile mentioning that only 10 min was required to observe a color change by the naked eye for $FF@PW_{12}$, but a longer time of 90 min was required for previous sandwich-type POMs based enzyme mimics.[40] Furthermore, the process was quantitatively monitored by recording TMB UV absorbance at 652 nm as shown in Figure 4a as reported previously.[40] Figure 4b shows that the intensity of $TMB/H_2O_2/FF@PW_{12}$ (dark cyan trace) was much higher than that of $TMB/H_2O_2/PW_{12}$ (blue trace), while other control groups, such as $TMB/H_2O_2/FF$ (dark yellow trace), $TMB/FF@PW_{12}$ (black trace), and $H_2O_2/FF@PW_{12}$ (red trace), remain clear under similar reaction conditions. These results indicate that the peroxidase-like activity of $FF@PW_{12}$ is higher than the catalytic performance of pristine PW_{12}. It is worth noting that the active sites on PW_{12} clusters are open to TMB and H_2O_2, leading to a

direct oxidation reaction. Thus, the mass transfer issue is almost negligible in a homogeneous phase. However, agglomeration occurred due to the strong electrostatic interactions between negatively charged PW_{12} and positively charged TMB at lower pH values. Thus, the active surface of PW_{12} may be blocked by adsorbed TMB, and the total concentration of TMB in solution will therefore decrease due to the severe sedimentation. At the end of the reaction, we always found blue precipitations at the bottom of the cuvette. In contrast, the reaction system of $TMB/H_2O_2/FF@PW_{12}$ was stable for a long aging time, in which no agglomeration was observed throughout the process.

The encapsulation of FF on the surface of PW_{12} will generate a smart microenvironment for the access of TMB and H_2O_2. It is well-known that higher affinity of TMB and H_2O_2 is beneficial in enhancing the catalytic performance of TMB oxidation reaction. Theoretically, there are noncovalent interactions of hydrogen bonding and $\pi-\pi$ stacking of aromatic moieties between FF and TMB, driving the movement of TMB toward composite spheres. Also, the surface charge of $FF@PW_{12}$ is measured to be −65 mV, which is of great importance for the capture of TMB. The ratio between FF and PW_{12} is 3:1 due to charge balance, as confirmed by the TGA analysis (Figure 2d). The loose packing of FF around catalytic sites, i.e. the PW_{12} clusters, will provide rational pathways for the movement of H_2O_2 toward sphere centers. That is to say, lower hydrophobicity of composite spheres is better to capture H_2O_2. We thus hypothesize that the peroxidase-like activity may be deteriorated by enhancing the hydrophobicity of the surface of the PW_{12} composites. As shown in Figure S6, SI, $PW_{12}@STAB$ (inset of Figure S6a) was constructed to create more hydrophobic surface, and tubular morphology is observed for the $STAB@PW_{12}$ composite as shown in Figure S6b. The static contact angle of the compressed film of the tubes is ~142°. As expected, no oxidation reaction was observed for the $STAB@PW_{12}$ composite as indicated by the clear color of TMB (Figure S7, SI), validating our hypothesis that the hydrophobic surface deteriorates the peroxidase-like activity of the system. Moreover, the affinity toward TMB in $STAB@PW_{12}$ was weakened due to the dense stacking of ordered alkyl chains, and this was proven by small angle and wide-angle X-ray diffraction shown in Figure S8, SI.

After careful evaluations of the peroxidase-like activity of the $FF@PW_{12}$ system shown in Figure S9, SI, the relative activity for 10 batches was ~13 times higher than that of pristine PW_{12} without any capping agents under similar reaction conditions. The enhanced catalytic performance is closely related to the synergistic effects of the integration of FF and PW_{12}. It is also worth mentioning that the introduction of FF not only enhances the heterogeneity of composite for recovery but also might improve the biocompatibility for bioapplications. Furthermore, comparing with the homogeneous media of pristine PW_{12}, in the present system, the metastable solution consisted of nanosized composite spheres which do not interfere with the observation by the naked eye or measurement by UV−vis microscopy. Thus, the present systems potentially may be used in many applications if POMs aggregates were assembled on a solid support such as graphene. Superior catalytic activity toward the oxidation reaction might be enhanced due to the presence of maximized synergistic effects.

In the past decade, large-scale production of GO is usually done by Hummer's method, and GO is an ideal support for anchoring nanosized species to avoid agglomerations or

maximize the synergistic effects among all components.[49,50] In the next part, we further construct the FF@PW$_{12}$@GO composite to enhance the peroxidase-like activity, intending to develop a promising candidate for practical implementation in peroxidase-like mimics. The spherical structures of FF@PW$_{12}$ are maintained on the surface of GO oxide, as confirmed by SEM and TEM in Figure 1c and 1d. The average size of submicrospheres is about 480 nm, smaller than that of FF@PW$_{12}$, indicating the confinement effect of GO on the spherical growth.[35] Raman results in Figure S10a show the characteristic peaks of PW$_{12}$, GO, and FF@PW$_{12}$@GO, indicating the successful integration of the spheres and GO. The I_D/I_G ratio increases from 0.87 (GO) to 0.97 (FF@PW$_{12}$@GO), confirming the partial reduction of GO. This is attributed to both contributions from the reduced activity of PW$_{12}$ to GO under laser exposure and laser intensity itself during Raman measurement.[51] Meanwhile, the deposition of FF@PW$_{12}$ leads to increased defects, disorder, and sp^2 domain sites on the graphene sheet due to electron movement from the PW$_{12}$ to graphene oxide.[52] Manifested Raman spectra in Figure S10b further confirms the characteristic peaks of PW$_{12}$ in ternary hybrids. The peroxidase-like activity was first investigated as a function of GO contents in the composite. As shown in Figure S11 of the SI, the highest signal was obtained when 5 wt % GO was introduced. The peroxidase-like activity of the FF@PW$_{12}$@GO (5 wt %) composite indeed exhibits higher absorbance in 10 min than that of FF@PW$_{12}$. The relative performance of FF@PW$_{12}$@GO is ~1.7 times higher than that of FF@PW$_{12}$ after performing comparisons for 10 batches as indicated in Figure S9 of SI. Higher contents of GO > 5 wt % may potentially cover the surface of FF@PW$_{12}$ spheres and hence block the accessible pathways of TMB or H$_2$O$_2$. Therefore, FF@PW$_{12}$@GO (5 wt %) was used to perform the following peroxidase-like evaluation study.

Similarly, experiments using HRP and other nanoenzyme systems show that their catalytic activity is highly dependent on the pH, temperature, catalyst amount, and H$_2$O$_2$ concentration, similar to the FF@PW$_{12}$@GO systems.[43,53,54] In this work, peroxidase-like activity of FF@PW$_{12}$@GO was evaluated via varying the catalyst amount from 3×10^{-3} mg/mL to 3×10^{-2} mg/mL and the H$_2$O$_2$ concentration from 1 to 1000 μM. The reaction equilibrated in 10 min when 1×10^{-2} mg/mL FF@PW$_{12}$@GO was applied. The pH dependence of the system was shown in Figure 5a with maximal intensity at pH ~ 3. It is clear that the catalytic activity of FF@PW$_{12}$@GO is much higher in

acidic media than neutral conditions, implying that the oxidation of TMB proceeds more easily under acidic conditions, consistent with pristine PW$_{12}$, HRP, and other nanoenzymes.[37] However, the catalytic activity of FF@PW$_{12}$@GO is lost when pH > 4.0, potentially due to the structural decomposition of the POMs. The temperature dependence of the reaction is also examined as shown in Figure 5b in which a direct correlation is observed. Unlike other systems that are sensitive to high temperature, FF@PW$_{12}$@GO still maintains its catalytic activity even at 60 °C. Too much high temperature will cause the fast decomposition of H$_2$O$_2$, leading to compromise the oxidation reaction of TMB.

The apparent steady-state kinetic parameters of FF@PW$_{12}$@GO are evaluated by changing the concentrations of TMB and H$_2$O$_2$ under the optimal condition. Basically, the kinetic data were acquired by varying one substrate concentration and fixing the other. As illustrated in Figure 6, the reaction demonstrates
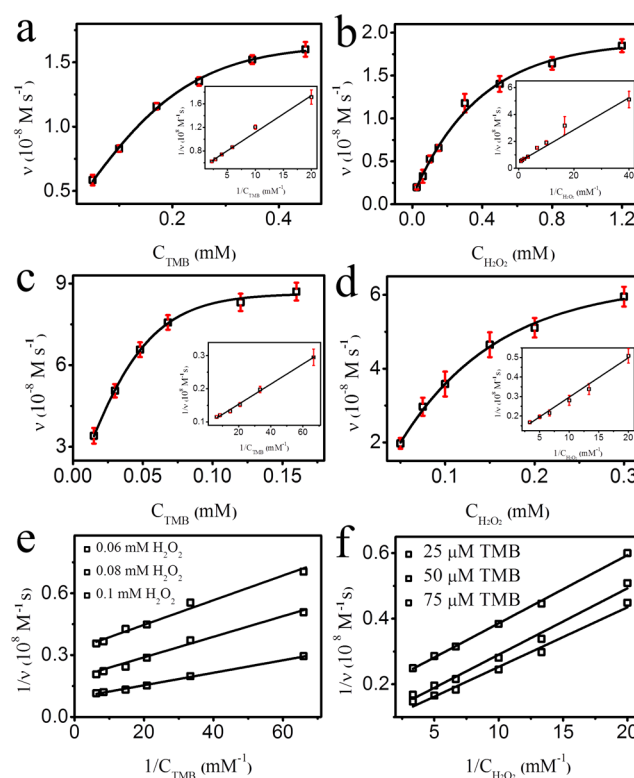
Figure 6. Steady-state kinetic assays of FF@PW$_{12}$ and FF@PW$_{12}$@GO. (a: FF@PW$_{12}$) and (c: FF@PW$_{12}$@GO) 80 μM H$_2$O$_2$ with varying TMB concentration, (b: FF@PW$_{12}$) and (d: FF@PW$_{12}$@GO) 50 μM TMB with varying H$_2$O$_2$ concentration. The reaction was performed in 0.1 M, pH = 3 buffer solution at 60 °C. (e and f) Double reciprocal plots of the activity of FF@PW$_{12}$@GO with respect to H$_2$O$_2$ or TMB concentration.

typical Michaelis−Menten kinetics within a certain range of substrate concentration. The K_m and V_{max} deduced from Lineweaver−Burk plots are summarized in Table S2. The apparent K_m value for FF@PW$_{12}$@GO (0.214 mM) using the H$_2$O$_2$ substrate is smaller than that of FF@PW$_{12}$ (0.257 mM), suggesting that FF@PW$_{12}$@GO has higher affinity for H$_2$O$_2$ than HRP. This is consistent with the result of the maximal activity of FF@PW$_{12}$ obtained at higher H$_2$O$_2$ concentration. In addition, the K_m value of FF@PW$_{12}$@GO (0.033 mM) using the TMB substrate is lower than that of FF@PW$_{12}$ (0.127
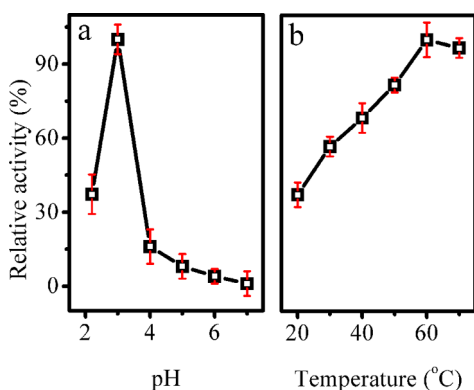

Figure 5. Dependence of the peroxidase-like activity on (a) pH (4.5, 5, 5.5, 6, and 6.5) and (b) temperature (20, 30, 40, 45, 50, 55, 60, and 65 °C).

mM), indicating that FF@PW$_{12}$@GO has a higher affinity for TMB than FF@PW$_{12}$. There are many advantages for the introduction of GO. 1) Previous reports proved that GO can be used as an ideal support for carrying antitumor drugs due to its good biocompatibility,[55] and this will expand the application of FF@PW$_{12}$@GO to biorelated fields. 2) GO possesses excellent absorption ability for dyes, allowing it to be used as efficient absorbents for removing dyes in aqueous solutions. This feature is beneficial to the capture of TMB molecules in solutions and thus contributes to the enhancement of the affinity between FF@PW$_{12}$@GO and TMB. 3) The strong ionic interaction or electron transfer interaction between PW$_{12}$ and GO will lead to the alteration of redox activity of PW$_{12}$, and these noncovalent interactions may enhance the peroxidase-like activity of the as-synthesized FF@PW$_{12}$@GO. 4) The synergistic effect resulting from the integration of three independent components in one system contributes to the overall enhancements in catalytic performance.

In order to elucidate the electronic interaction between partially reduced GO and PW$_{12}$, a four-probe Hall measurement via the van der Pauw method was carried out at room temperature for the rGO film (reduced by 47 wt % HI solution, for conveniently electrochemical measurement) and the PW$_{12}$ decorated rGO film and compared carrier type, carrier mobilities, and carrier concentrations of each film in Table S3. All the samples are cut into the same size of 0.5 × 0.5 cm, and each film has been analyzed triply. As confirmed by the Hall measurement, all films were found to exhibit p-type behavior in which the major carrier was holes. The high carrier density of ~10^{15} was possibly originating from the effects of multilayer graphene. It is well-known that the rGO film is P-doped in ambient caused by the doping effect of the adsorbed moisture/oxygen and the substrate impurities.[56] In addition, the LUMO energy of PW$_{12}$ is about −4.79 eV, which is lower than that of graphene (−4.3 eV). The matching energy level facilitates the electron transport from graphene to the LUMO orbitals of PW$_{12}$ due to the favorably thermodynamic driving force for electron transfer. It is also known that POMs possess superior ability of maintaining intact structure after accepting a certain amount of electrons, acting as electron reservoir. The rGO film was significantly P-doped after being decorated by PW$_{12}$, showing enhanced carrier mobility of 2.58 cm^2/(V s) (SD: 0.01 cm^2/(V s)) compared with that of the rGO film (2.30 cm^2/(V s) with SD of 0.04 cm^2/(V s)).[51]

Furthermore, as shown in Figure 7 (black trace), the cyclic voltammogram (CV) of PW$_{12}$ in 1 M H$_2$SO$_4$ gives rise to three couples of redox waves in the potential range from +0.25 to −0.7 V. The mean peak potential $E_{1/2} = (E_{pa}+E_{pc})/2$ are 0.053 V (I), − 0.218 V (II), and −0.562 V (III), respectively, which are nearly the same as those observed from the solution electrochemistry of PW$_{12}$.[57] In contrast, $E_{1/2}$ values of PW$_{12}$ on the GC@3DG electrode are 0.044 V (I), − 0.229 V (II), and −0.559 V (III), respectively. As summarized in Table S4, the oxidation waves E_{pa} are almost unchanged, while the reduction waves E_{pc} shift to a more negative potential (I: from 0.023 to 0 V; II: from −0.247 to −0.276 v; III: from −0.582 to −0.595 V). These observations suggest that 3DG causes significant influence on the electronic structure of the reduced forms of the redox couples of PW$_{12}$ due to PW$_{12}$ energy level stabilization, which is ascribed to electrostatic interaction and charge transfer interaction between PW$_{12}$ and graphene surface.[52,58] Taken together, strong interactions between rGO and PW$_{12}$ indeed occurred and will significantly alter the redox
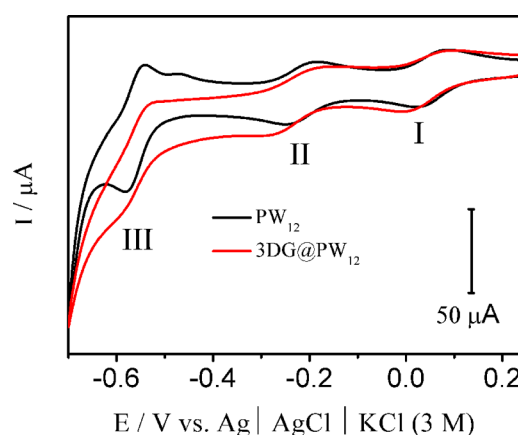

Figure 7. (A) Cyclic voltammograms of 1 mg/mL PW$_{12}$ on GC (a: black trace) and GC@3DG electrodes (b: red trace) in 1 M H$_2$SO$_4$ aqueous solution, scan rate 100 mV/s.

properties of PW$_{12}$ toward the oxidation of TMB in the presence of H$_2$O$_2$.

In addition, the nature of the TMB catalytic reaction may originate from the generation of the hydroxyl radical ($^{\bullet}$OH) from the decomposition of H$_2$O$_2$. The terephthalic acid (TA) photoluminescence probing technique, which is widely applied in detecting the hydroxyl radical due to high sensitivity and selectivity, was therefore used to confirm the formation of $^{\bullet}$OH.[59] Nonluminescent TA is converted to highly fluorescent 2-hydroxy terephthalic acid (HTA) in the presence of FF@PW$_{12}$@GO. In the process, HTA is a product of TA reacted with $^{\bullet}$OH. As shown in Figure S12 of the SI, the fluorescence intensity of the solution containing FF@PW$_{12}$@GO is 17 times higher than that in the absence of FF@PW$_{12}$@GO, indicating that our hybrid could activate H$_2$O$_2$ to generate $^{\bullet}$OH. Two steps are speculated to be involved in the oxidation reaction of TMB. H$_2$O$_2$ molecules are first adsorbed to FF@PW$_{12}$@GO and then get activated by the synergistic effects of the three components. Furthermore, the fluorescence intensity of the solution containing FF@PW$_{12}$ is lower than that of FF@PW$_{12}$@GO, suggesting that less $^{\bullet}$OH is generated in the former case, consistent with the difference of peroxidase-like activities of these two systems. Furthermore, as shown in Figure 8, the results of ESR experiments in the systems of FF@PW$_{12}$@GO−
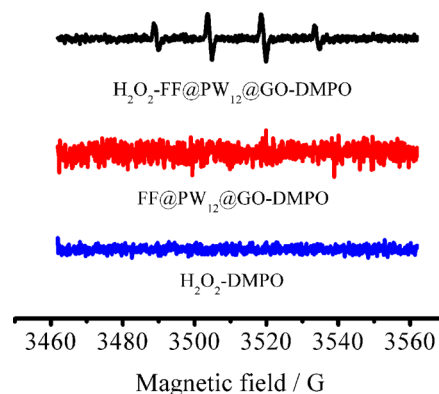

Figure 8. Spin-trapping ESR spectra of $^{\bullet}$OH radicals in the system of H$_2$O$_2$−FF@PW$_{12}$@GO−DMPO, FF@PW$_{12}$@GO−DMPO, and H$_2$O$_2$−DMPO. Conditions: 15 mM DMPO, 3 mM H$_2$O$_2$, 1 mg mL^{-1} FF@PW$_{12}$@GO, and 0.1 M NaAc buffer.

DMPO and H_2O_2−DMPO indicate that no characteristic peaks of the typical DMPO−•OH adduct were observed. In contrast, the ESR spectrum in the system of H_2O_2−FF@PW_{12}@GO− DMPO displayed a 4-fold characteristic peak of the typical DMPO−•OH adduct with an intensity ratio of 1:2:2:1, demonstrating that FF@PW_{12}@GO could convert H_2O_2 to •OH radicals.[60] ESR results further confirmed that FF@PW_{12}@ GO possesses peroxidase-mimic activity. It is also well-known that tungstate in PW_{12} can be oxidized to a peroxotungstate such as $[W_2O_3(O_2)_4]^{2-}$ and $\{PO_4[WO(O_2)_2]_4\}^{3-}$ by H_2O_2.[61−63] Subsequently, the resultant peroxo species possessing a strong oxidation ability acts as a real catalyst to sufficiently catalyze the oxidation of TMB. As shown in Figure S13, the Raman spectrum of FF@PW_{12}@GO incubated in 80 μM H_2O_2 showed a new peak at ∼845 cm^{-1} corresponding to ν(O−O) according to the assignment for the peroxide bond.[64] Meanwhile, the peroxo species can also accelerate the formation of free radicals by the disassociation of hydrogen peroxide. Both ways might contribute to the oxidation of TMB to produce a blue solution. As shown in Figure 5b, at an elevated temperature around 60 °C, the formation speed of peroxotungstate and •OH will be greatly enhanced. In addition, high temperature will loose the supramolecular sphere in comparison with that under low temperature, facilitating the entrance of H_2O_2 and TMB. Taken together, those effects greatly accelerated the oxidation reaction of TMB in the presence of H_2O_2.

To further understand the mechanism of the catalysis property of FF@PW_{12}@GO, the peroxidase-like activity over a range of TMB and H_2O_2 concentrations was performed. As shown in Figure 6e and 6f, the double reciprocal plots of initial velocity versus concentration of one substrate were acquired over a range of concentrations of the second substrate. The slopes of the plots are almost parallel, indicating a possible ping-pong mechanism. A leaching experiment was carried out to rule out the possibility that the oxidation is governed by the leached PW_{12} polyoxoanion. FF@PW_{12}@GO was incubated in buffer solution for 30 min at 60 °C under ultrasonication. Subsequently, the supernatant after centrifugation was used for measurement. No characteristic peak of oxidized TMB is seen in Figure S14 of the SI, indicating the absence of oxidized TMB in the supernatant, and the peroxidase-like activity originates from FF@PW_{12}@GO rather than the leached PW_{12} polyoxoanion.

It is well-known that natural enzyme activity will be severely deteriorated under thermal heating. For example, the enzyme activity of HRP dramatically declined after treatment at a temperature higher than 40 °C after 2 h. In contrast, the enzyme activity of compound FF@PW_{12}@GO is stable when it was incubated at a wide range of temperatures from 20 to 70 °C for 12 h as shown in Figure 5b. The stability of the hybrid compounds was further examined by Raman spectra before and after reaction. The characteristic bands of the PW_{12} cluster are maintained in a recycled catalyst after 10 runs. The slight peak position differences are attributed to the slightly structural distortion of POMs during treatment. The robustness of composite at higher temperature and pH value make them promising materials for a broad application in biodetection.

Colorimetric detection of H_2O_2 was realized from the color change of TMB solution. As shown in Figure 9, absorbance intensity plateaus after adding 75 μM H_2O_2. The linear scale for H_2O_2 was varied from 1×10^{-6} to 75×10^{-6} mol L^{-1} within the limit of detection (LOD) of 0.11 μM (LOD = KS_0/S, where
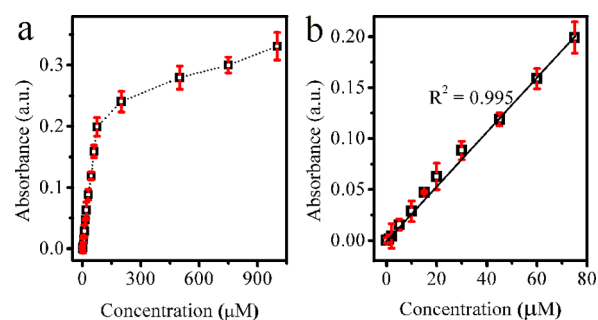

Figure 9. H_2O_2 detection measurement. a) UV−vis intensity of TMB at 652 nm demonstrating the concentration dependence of H_2O_2 from 1 μM to 1000 μM and b) linear fit of the absorption intensity from a) in the concentration from 1 μM to 75 μM.

K is a numerical factor determined by the desirable confidence level, S_0 is the standard deviation (SD) of the blank measurements ($n = 10$, $K = 3$), and S is the slope of the calibration curve).[65] The LOD of our detection method is higher than that of GO[28] (0.05 μM) but lower than the method using PW_{12}[37] (0.134 μM), SiW_{12}[38] (0.4 μM), Fe_3O_4 nanoparticles[66] (3 μM), and Au nanoparticles[67] (0.5 μM), implying the superiority for potential application as the H_2O_2 detector.

■ CONCLUSIONS

In summary, the ternary hybrid FF@PW_{12}@GO has been successfully prepared via a facile coassembly method. This handy ternary hybrid endows the product with four characteristics: 1) the electrostatic interactions between FF and POMs facilitate catalysis in the more efficient heterogeneous phase; 2) GO possesses excellent absorption ability for TMB, contributing to the enhancement of the affinity between FF@PW_{12}@ GO and TMB; 3) the strong ionic interaction or electron transfer interaction between PW_{12} and GO improves peroxidase-like activity further, and such strong interactions have been solidly confirmed by Hall measurement and CV measurement; 4) the synergistic effect resulted from the integration of three independent components in one system contributing to the overall catalytic performance. Experimental data reveals the composition and distribution of PW_{12} in FF@ PW_{12} as homogeneous submicrospheres with noncovalent interactions between individual components. The as-prepared FF@PW_{12}@GO(5 wt %) exhibits interesting peroxidase-like activity using TMB as a colorimetric substrate, 1.7 times higher than that of PW_{12}@FF without GO and 13 times higher than that of pristine PW_{12} without any encapsulating agents. Through the comparison study of STAB@PW_{12}, which has a hydrophobic surface and dense packing of alkyl chains, it is confirmed that the high affinity of the ternary hybrid toward TMB and H_2O_2 is justified by optimizing the structural composition. Last but not least, PW_{12}@FF@GO can be used to detect H_2O_2 within the limit of detection of 0.11 μM in the range of 1−75 μM. This method indeed describes a facile route to a high performance peroxidase-like mimic for medical diagnostics and biotechnology.

■ ASSOCIATED CONTENT

ⓢ Supporting Information

The Supporting Information is available free of charge on the ACS Publications website at DOI: 10.1021/acsami.5b07046.

Figures S1−S16 and Tables S1−S4 (PDF)

■ AUTHOR INFORMATION

Corresponding Authors

*E-mail: qiuyf@hit.edu.cn (Y.Q.).

*Phone: 86 451 86403583. Fax: 86 451 86403583. E-mail: hupa@hit.edu.cn (P.H.).

*E-mail: beverlyzh@berkeley.edu (C.Z.).

Author Contributions

Z.M., Y.F.Q., and P.A.H. conceived the experiments, Z.M. and Y.F.Q. designed and conducted the coassembly, peroxidase-like experiments, CV, SEM, and TEM experiments, H.H.Y. conducted the UV−vis measurement, J.J.L. and Y.L. conducted the graphene synthesis, Y.M.H. performed the Hall measurement. Z.M., Y.F.Q., and P.A.H. analyzed the results, Z.M., Y.F.Q.. and C.Z wrote the manuscript. All the authors reviewed and approved the manuscript.

Notes

The authors declare no competing financial interest.

■ REFERENCES

(1) Whitesides, G. M.; Grzybowski, B. Self-Assembly at All Scales. *Science* **2002**, *295*, 2418−2421.

(2) Chakrabarty, R.; Mukherjee, P. S.; Stang, P. J. Supramolecular Coordination: Self-Assembly of Finite Two-and Three-Dimensional Ensembles. *Chem. Rev.* **2011**, *111*, 6810−6918.

(3) Dong, H.; Dube, N.; Shu, J. Y.; Seo, J. W.; Mahakian, L. M.; Ferrara, K. W.; Xu, T. Long-Circulating 15 nm Micelles Based on Amphiphilic 3-Helix Peptide−PEG Conjugates. *ACS Nano* **2012**, *6*, 5320−5329.

(4) Yan, X.; Zhu, P.; Fei, J.; Li, J. Self-Assembly of Peptide-Inorganic Hybrid Spheres for Adaptive Encapsulation of Guests. *Adv. Mater.* **2010**, *22*, 1283−1287.

(5) Ryan, K.; Beirne, J.; Redmond, G.; Kilpatrick, J. I.; Guyonnet, J.; Buchete, N.-V.; Kholkin, A. L.; Rodriguez, B. J. Nanoscale Piezoelectric Properties of Self-Assembled Fmoc−FF Peptide Fibrous Networks. *ACS Appl. Mater. Interfaces* **2015**, *7*, 12702−12707.

(6) Biswas, K.; Rao, C. N. R. Nanostructured Peptide Fibrils Formed at the Organic−Aqueous Interface and Their Use as Templates to Prepare Inorganic Nanostructures. *ACS Appl. Mater. Interfaces* **2009**, *1*, 811−815.

(7) Cheng, C.; Tang, M.-C.; Wu, C.-S.; Simon, T.; Ko, F.-H. New Synthesis Route of Hydrogel through a Bioinspired Supramolecular Approach: Gelation, Binding Interaction, and in Vitro Dressing. *ACS Appl. Mater. Interfaces* **2015**, *7*, 19306−19315.

(8) Taskin, M. B.; Sasso, L.; Dimaki, M.; Svendsen, W. E.; Castillo-León, J. Combined Cell Culture-Biosensing Platform Using Vertically Aligned Patterned Peptide Nanofibers for Cellular Studies. *ACS Appl. Mater. Interfaces* **2013**, *5*, 3323−3328.

(9) Bai, Y.; Zhang, G.-Q.; Dang, D.-B.; Ma, P.-T.; Gao, H.; Niu, J.-Y. Assembly of Polyoxometalate-Based Inorganic−Organic Compounds from Silver−Schiff Base Building Blocks: Synthesis, Crystal Structures and Luminescent Properties. *CrystEngComm* **2011**, *13*, 4181−4187.

(10) Song, Y. F.; Long, D. L.; Ritchie, C.; Cronin, L. Nanoscale Polyoxometalate-Based Inorganic/Organic Hybrids. *Chem. Rec.* **2011**, *11*, 158−171.

(11) Li, W.; Xia, F.; Qu, J.; Li, P.; Chen, D.; Chen, Z.; Yu, Y.; Lu, Y.; Caruso, R. A.; Song, W. Versatile Inorganic-Organic Hybrid WO$_X$-Ethylenediamine Nanowires: Synthesis, Mechanism and Application in Heavy Metal Ion Adsorption and Catalysis. *Nano Res.* **2014**, *7*, 903−916.

(12) Shi, Y.; Wan, Y.; Zhao, D. Ordered Mesoporous Non-Oxide Materials. *Chem. Soc. Rev.* **2011**, *40*, 3854−3878.

(13) Wang, E. B.; Hu, C. W.; Xu, L. *Concise of Polyoxometalate Chemistry*; Chemical Industry Press: Beijing, 1998.

(14) Faul, C. F.; Antonietti, M. Ionic Self-Assembly: Facile Synthesis of Supramolecular Materials. *Adv. Mater.* **2003**, *15*, 673−683.

(15) Ma, M.; Chen, H.; Chen, Y.; Wang, X.; Chen, F.; Cui, X.; Shi, J. Au Capped Magnetic Core/Mesoporous Silica Shell Nanoparticles for Combined Photothermo-/Chemo-Therapy and Multimodal Imaging. *Biomaterials* **2012**, *33*, 989−998.

(16) Serna, P.; Gates, B. C. Molecular Metal Catalysts on Supports: Organometallic Chemistry Meets Surface Science. *Acc. Chem. Res.* **2014**, *47*, 2612−2620.

(17) Li, W.; Zhao, D. Extension of the Stöber Method to Construct Mesoporous SiO$_2$ and TiO$_2$ Shells for Uniform Multifunctional Core−Shell Structures. *Adv. Mater.* **2013**, *25*, 142−149.

(18) Jin, H.; Heller, D. A.; Kalbacova, M.; Kim, J.-H.; Zhang, J.; Boghossian, A. A.; Maheshri, N.; Strano, M. S. Detection of Single-Molecule H$_2$O$_2$ Signalling from Epidermal Growth Factor Receptor Using Fluorescent Single-Walled Carbon Nanotubes. *Nat. Nanotechnol.* **2010**, *5*, 302−309.

(19) Wei, H.; Wang, E. Fe$_3$O$_4$ Magnetic Nanoparticles as Peroxidase Mimetics and Their Applications in H$_2$O$_2$ and Glucose Detection. *Anal. Chem.* **2008**, *80*, 2250−2254.

(20) Gao, L.; Zhuang, J.; Nie, L.; Zhang, J.; Zhang, Y.; Gu, N.; Wang, T.; Feng, J.; Yang, D.; Perrett, S.; Yan, X. Intrinsic Peroxidase-Like Activity of Ferromagnetic Nanoparticles. *Nat. Nanotechnol.* **2007**, *2*, 577−583.

(21) Olucha, F.; Martínez-García, F.; López-García, C. A New Stabilizing Agent for the Tetramethyl Benzidine (TMB) Reaction Product in the Histochemical Detection of Horseradish Peroxidase (HRP). *J. Neurosci. Methods* **1985**, *13*, 131−138.

(22) Mateo, C.; Palomo, J. M.; Fernandez-Lorente, G.; Guisan, J. M.; Fernandez-Lafuente, R. Improvement of Enzyme Activity, Stability and Selectivity Via Immobilization Techniques. *Enzyme Microb. Technol.* **2007**, *40*, 1451−1463.

(23) Veitch, N. C. Horseradish Peroxidase: A Modern View of a Classic Enzyme. *Phytochemistry* **2004**, *65*, 249−259.

(24) Wei, H.; Wang, E. Nanomaterials with Enzyme-Like Characteristics (Nanozymes): Next-Generation Artificial Enzymes. *Chem. Soc. Rev.* **2013**, *42*, 6060−6093.

(25) Jiang, X.; Sun, C.; Guo, Y.; Nie, G.; Xu, L. Peroxidase-Like Activity of Apoferritin Paired Gold Clusters for Glucose Detection. *Biosens. Bioelectron.* **2015**, *64*, 165−170.

(26) Zhang, L.; Han, L.; Hu, P.; Wang, L.; Dong, S.; TiO2 Nanotube. Arrays: Intrinsic Peroxidase Mimetics. *Chem. Commun.* **2013**, *49*, 10480−10482.

(27) Zhang, J.-W.; Zhang, H.-T.; Du, Z.-Y.; Wang, X.; Yu, S.-H.; Jiang, H.-L. Water-Stable Metal-Organic Frameworks with Intrinsic Peroxidase-Like Catalytic Activity as a Colorimetric Biosensing Platform. *Chem. Commun.* **2014**, *50*, 1092−1094.

(28) Song, Y.; Qu, K.; Zhao, C.; Ren, J.; Qu, X. Graphene Oxide: Intrinsic Peroxidase Catalytic Activity and Its Application to Glucose Detection. *Adv. Mater.* **2010**, *22*, 2206−2210.

(29) Liu, M.; Zhao, H.; Chen, S.; Yu, H.; Quan, X. Stimuli-Responsive Peroxidase Mimicking at a Smart Graphene Interface. *Chem. Commun.* **2012**, *48*, 7055−7057.

(30) Tao, Y.; Ju, E.; Ren, J.; Qu, X. Polypyrrole Nanoparticles as Promising Enzyme Mimics for Sensitive Hydrogen Peroxide Detection. *Chem. Commun.* **2014**, *50*, 3030−3032.

(31) Asati, A.; Santra, S.; Kaittanis, C.; Nath, S.; Perez, J. M. Oxidase-Like Activity of Polymer-Coated Cerium Oxide Nanoparticles. *Angew. Chem., Int. Ed.* **2009**, *48*, 2308−2312.

(32) He, D.; Jiang, Y.; Lv, H.; Pan, M.; Mu, S. Nitrogen-Doped Reduced Graphene Oxide Supports for Noble Metal Catalysts with Greatly Enhanced Activity and Stability. *Appl. Catal., B* 2013, *132-133*, 379−388.

(33) Liang, Y.; Li, Y.; Wang, H.; Zhou, J.; Wang, J.; Regier, T.; Dai, H. Co_3O_4 Nanocrystals on Graphene as a Synergistic Catalyst for Oxygen Reduction Reaction. *Nat. Mater.* 2011, *10*, 780−786.

(34) Chen, Z.; Ren, W.; Gao, L.; Liu, B.; Pei, S.; Cheng, H.-M. Three-Dimensional Flexible and Conductive Interconnected Graphene Networks Grown by Chemical Vapour Deposition. *Nat. Mater.* 2011, *10*, 424−428.

(35) He, P.; Xu, B.; Wang, P. p.; Liu, H.; Wang, X. A Monolayer Polyoxometalate Superlattice. *Adv. Mater.* 2014, *26*, 4339−4344.

(36) Tao, Y.; Lin, Y.; Huang, Z.; Ren, J.; Qu, X. Incorporating Graphene Oxide and Gold Nanoclusters: A Synergistic Catalyst with Surprisingly High Peroxidase-Like Activity over a Broad pH Range and Its Application for Cancer Cell Detection. *Adv. Mater.* 2013, *25*, 2594−2599.

(37) Wang, J.; Han, D.; Wang, X.; Qi, B.; Zhao, M. Polyoxometalates as Peroxidase Mimetics and Their Applications in H_2O_2 and Glucose Detection. *Biosens. Bioelectron.* 2012, *36*, 18−21.

(38) Liu, S.; Tian, J.; Wang, L.; Zhang, Y.; Luo, Y.; Li, H.; Asiri, A. M.; Al-Youbi, A. O.; Sun, X. Fast and Sensitive Colorimetric Detection of H_2O_2 and Glucose: A Strategy Based on Polyoxometalate Clusters. *ChemPlusChem* 2012, *77*, 541−544.

(39) Li, D.; Han, H.; Wang, Y.; Wang, X.; Li, Y.; Wang, E. Modification of Tetranuclear Zirconium-Substituted Polyoxometalates-Syntheses, Structures, and Peroxidase-Like Catalytic Activities. *Eur. J. Inorg. Chem.* 2013, *2013*, 1926−1934.

(40) Sun, C.; Chen, X.; Xu, J.; Wei, M.; Wang, J.; Mi, X.; Wang, X.; Wu, Y.; Liu, Y. Fabrication of an Inorganic-Organic Hybrid Based on an Iron-Substituted Polyoxotungstate as a Peroxidase for Colorimetric Immunoassays of H_2O_2 and Cancer Cells. *J. Mater. Chem. A* 2013, *1*, 4699−4705.

(41) Wang, J.; Mi, X.; Guan, H.; Wang, X.; Wu, Y. Assembly of Folate-Polyoxometalate Hybrid Spheres for Colorimetric Immunoassay Like Oxidase. *Chem. Commun.* 2011, *47*, 2940−2942.

(42) Li, X.; Wang, Z.; Qiu, Y.; Pan, Q.; Hu, P. 3D Graphene/ZnO Nanorods Composite Networks as Supercapacitor Electrodes. *J. Alloys Compd.* 2015, *620*, 31−37.

(43) Gao, L.; Zhuang, J.; Nie, L.; Zhang, J.; Zhang, Y.; Gu, N.; Wang, T.; Feng, J.; Yang, D.; Perrett, S.; Yan, X. Intrinsic Peroxidase-Like Activity of Ferromagnetic Nanoparticles. *Nat. Nanotechnol.* 2007, *2*, 577−583.

(44) Li, K.; Hu, J.; Li, W.; Ma, F.; Xu, L.; Guo, Y. Design of Mesostructured $H_3PW_{12}O_{40}$-Silica Materials with Controllable Ordered and Disordered Pore Geometries and Their Application for the Synthesis of Diphenolic Acid. *J. Mater. Chem.* 2009, *19*, 8628−8638.

(45) Li, H.; Sun, H.; Qi, W.; Xu, M.; Wu, L. Onionlike Hybrid Assemblies Based on Surfactant-Encapsulated Polyoxometalates. *Angew. Chem., Int. Ed.* 2007, *46*, 1300−1303.

(46) Görbitz, C. H. The Structure of Nanotubes Formed by Diphenylalanine, the Core Recognition Motif of Alzheimer's β-Amyloid Polypeptide. *Chem. Commun.* 2006, 2332−2334.

(47) Reches, M.; Gazit, E. Controlled Patterning of Aligned Self-Assembled Peptide Nanotubes. *Nat. Nanotechnol.* 2006, *1*, 195−200.

(48) Nisar, A.; Zhuang, J.; Wang, X. Construction of Amphiphilic Polyoxometalate Mesostructures as a Highly Efficient Desulfurization Catalyst. *Adv. Mater.* 2011, *23*, 1130−1135.

(49) Li, D.; Müller, M. B.; Gilje, S.; Kaner, R. B.; Wallace, G. G. Processable Aqueous Dispersions of Graphene Nanosheets. *Nat. Nanotechnol.* 2008, *3*, 101−105.

(50) Yang, S.; Cao, C.; Li, G.; Sun, Y.; Huang, P.; Wei, F.; Song, W. Improving the Electrochemical Performance of Fe_3O_4 Nanoparticles Via a Double Protection Strategy through Carbon Nanotube Decoration and Graphene Networks. *Nano Res.* 2015, *8*, 1339−1347.

(51) Li, H.; Pang, S.; Wu, S.; Feng, X.; Müllen, K.; Bubeck, C. Layer-by-Layer Assembly and Uv Photoreduction of Graphene−Polyoxometalate Composite Films for Electronics. *J. Am. Chem. Soc.* 2011, *133*, 9423−9429.

(52) Kim, Y.; Shanmugam, S. Polyoxometalate−Reduced Graphene Oxide Hybrid Catalyst: Synthesis, Structure, and Electrochemical Properties. *ACS Appl. Mater. Interfaces* 2013, *5*, 12197−12204.

(53) Wei, H.; Wang, E. Nanomaterials with Enzyme-Like Characteristics (Nanozymes): Next-Generation Artificial Enzymes. *Chem. Soc. Rev.* 2013, *42*, 6060−6093.

(54) Lin, Y.; Ren, J.; Qu, X. Catalytically Active Nanomaterials: A Promising Candidate for Artificial Enzymes. *Acc. Chem. Res.* 2014, *47*, 1097−1105.

(55) Yang, K.; Wan, J.; Zhang, S.; Zhang, Y.; Lee, S.-T.; Liu, Z. In Vivo Pharmacokinetics, Long-Term Biodistribution, and Toxicology of Pegylated Graphene in Mice. *ACS Nano* 2011, *5*, 516−522.

(56) Zhang, W.; Chuu, C.-P.; Huang, J.-K.; Chen, C.-H.; Tsai, M.-L.; Chang, Y.-H.; Liang, C.-T.; Chen, Y.-Z.; Chueh, Y.-L.; He, J.-H. Ultrahigh-Gain Photodetectors Based on Atomically Thin Graphene-Mos2 Heterostructures. *Sci. Rep.* 2014, *4*, 3826.

(57) Sadakane, M.; Steckhan, E. Electrochemical Properties of Polyoxometalates as Electrocatalysts. *Chem. Rev.* 1998, *98*, 219−238.

(58) Kim, Y.; Ketpang, K.; Jaritphun, S.; Park, J. S.; Shanmugam, S. A Polyoxometalate Coupled Graphene Oxide−Nafion Composite Membrane for Fuel Cells Operating at Low Relative Humidity. *J. Mater. Chem. A* 2015, *3*, 8148−8155.

(59) Hu, A.-L.; Liu, Y.-H.; Deng, H.-H.; Hong, G.-L.; Liu, A.-L.; Lin, X.-H.; Xia, X.-H.; Chen, W. Fluorescent Hydrogen Peroxide Sensor Based on Cupric Oxide Nanoparticles and Its Application for Glucose and L-Lactate Detection. *Biosens. Bioelectron.* 2014, *61*, 374−378.

(60) Su, H.; Liu, D.-D.; Zhao, M.; Hu, W.-L.; Xue, S.-S.; Cao, Q.; Le, X.-Y.; Ji, L.-N.; Mao, Z.-W. Dual-Enzyme Characteristics of Polyvinylpyrrolidone-Capped Iridium Nanoparticles and Their Cellular Protective Effect against H2o2-Induced Oxidative Damage. *ACS Appl. Mater. Interfaces* 2015, *7*, 8233−8242.

(61) Ishimoto, R.; Kamata, K.; Mizuno, N. A Highly Active Protonated Tetranuclear Peroxotungstate for Oxidation with Hydrogen Peroxide. *Angew. Chem.* 2012, *124*, 4740−4743.

(62) Liu, L.; Chen, C.; Hu, X.; Mohamood, T.; Ma, W.; Lin, J.; Zhao, J. A Role of Ionic Liquid as an Activator for Efficient Olefin Epoxidation Catalyzed by Polyoxometalate. *New J. Chem.* 2008, *32*, 283−289.

(63) Ma, Z.; Wang, W.; Wu, Y.; He, Y.; Wu, T. Oxidative Degradation of Chitosan to the Low Molecular Water-Soluble Chitosan over Peroxotungstate as Chemical Scissors. *PLoS One* 2014, *9*, e100743.

(64) Nojima, S.; Kamata, K.; Suzuki, K.; Yamaguchi, K.; Mizuno, N. Selective Oxidation with Aqueous Hydrogen Peroxide by [Po4 {Wo (O2) 2} 4] 3− Supported on Zinc-Modified Tin Dioxide. *ChemCatChem* 2015, *7*, 1097−1104.

(65) Chen, J.; Chen, H.; Zhou, C.; Xu, J.; Yuan, F.; Wang, L. An Efficient Upconversion Luminescence Energy Transfer System for Determination of Trace Amounts of Nitrite Based on Nayf4:Yb3+, Er3+ as Donor. *Anal. Chim. Acta* 2012, *713*, 111−114.

(66) Wei, H.; Wang, E. Fe3o4Magnetic Nanoparticles as Peroxidase Mimetics and Their Applications in H2o2 and Glucose Detection. *Anal. Chem.* 2008, *80*, 2250−2254.

(67) Jv, Y.; Li, B.; Cao, R. Positively-Charged Gold Nanoparticles as Peroxidiase Mimic and Their Application in Hydrogen Peroxide and Glucose Detection. *Chem. Commun.* 2010, *46*, 8017−8019.